

# On-orbit calibration and performance of NOAA-20 VIIRS reflective solar bands

Kevin Twedt, Ning Lei, Xiaoxiong Xiong, Amit Angal, Sherry Li, Tiejun Chang, and Junqiang Sun

**Abstract**—The NOAA-20 (N20) satellite was launched on November 18, 2017 carrying the second Visible Infrared Imaging Radiometer Suite (VIIRS) instrument. Immediately following launch, the VIIRS passed a series of intensive calibration and validation tests, after which regular calibration and operation activities have continued successfully for more than three years. The production of NASA Collection 2 Level 1B (C2 L1B) for N20 VIIRS began in summer 2019. In this paper, we evaluate the early mission performance of the N20 VIIRS reflective solar bands (RSB) covering the first three full years of operation. The calibrated RSB gains are calculated primarily from the on-board solar diffuser and used in generating the C2 L1B reflectance and radiance products. We also show the on-orbit performance of the instrument noise, signal-to-noise ratio (SNR) and a reflectance uncertainty assessment. Comparisons are made to the first three years of operation of the first VIIRS instrument, aboard the Suomi National Polar-orbiting Partnership (SNPP) satellite. We evaluate the long-term stability of the calibrated N20 RSB reflectance product by looking at the long-term trends of lunar observations and data from the pseudo-invariant Libya 4 desert site. The N20 RSB have had excellent early mission performance, with changes in gain of less than 0.5% in the first three years across all detectors, stable L1B reflectance, and very stable values of detector SNR and reflectance uncertainty.

**Index Terms**—calibration, reflective solar bands, VIIRS, solar diffuser

## I. INTRODUCTION

THE Visible Infrared Imaging Radiometer Suite (VIIRS) launched on November 18, 2017 aboard the NOAA-20 (N20) satellite is the second VIIRS instrument, following the first one aboard the Suomi National Polar-orbiting Partnership (SNPP) satellite launched on October 28, 2011. The VIIRS instruments, as part of the Joint Polar Satellite System (JPSS) program, are an important part of NOAA's set of remote sensing instruments for weather and climate monitoring. Three more VIIRS instruments are planned for launch on future JPSS satellites. N20 was launched into a sun-synchronous polar orbit with an ascending node local equator crossing time of 13:25. The orbital path is the same as SNPP, so that the two operating VIIRS instruments view the same location on the Earth about 50 minutes apart [1].

The VIIRS instrument is a whiskbroom multi-band scanning radiometer that provides valuable imagery of the Earth's land,

ocean, atmosphere, and cryosphere with daily global coverage. There are 22 spectral bands spanning the visible through long-wave infrared wavelengths, with 14 reflective solar bands (RSB), 7 thermal emissive bands (TEB) and a panchromatic day night band (DNB) [2]–[5]. In the first few months after N20 launch, a series of intensive post-launch tests and calibrations were performed to validate the performance of the VIIRS instrument [6], [7]. After the initial characterization phase, regular calibration and operation activities have continued for more than three years. This paper focuses on the VIIRS RSB, which are calibrated on-orbit by use of an on-board solar diffuser (SD), with an SD stability monitor (SDSM) used to track the degradation of the SD [8]–[10]. SD calibrations are performed every orbit as the spacecraft crosses over the South Pole. Near-monthly lunar observations also aid in tracking and correcting for any long-term drift in the calibration stability.

For both SNPP [11] and N20 VIIRS, NASA maintains a set of public VIIRS data products for use by the NASA Earth science community as an additional resource to supplement the NOAA VIIRS data [12]. The N20 VIIRS NASA Collection 2 Level 1B (C2 L1B) data product began production around August 2019 and is available as Archive Set 5200 from NASA Level-1 Atmosphere Archive and Distribution System (LAADS). The calibration for RSB, DNB, and TEB is maintained by the VIIRS Characterization Support Team (VCST) [13]–[15]. The L1B serves as the baseline calibrated reflectance and radiance imagery for the higher-level land and atmosphere science and environmental data products, similar to what are currently available for SNPP VIIRS and Terra and Aqua MODIS.

We recently reviewed the N20 VIIRS SD and SDSM performance, and the VCST algorithms for the SD-based calibration [13]. We continue that analysis in this paper, presenting an evaluation of the early mission performance of the VIIRS RSB and the calibrated RSB gains that are used in generating the N20 VIIRS C2 L1B reflectance and radiance products. We also show the on-orbit performance of the instrument noise and signal-to-noise ratio (SNR) and show an uncertainty assessment for the top-of-atmosphere reflectance product. We evaluate the long-term stability of the calibrated N20 RSB reflectance product by looking at the long-term trends of the lunar observations and the data from the pseudo-invariant

K. Twedt, N. Lei, A. Angal, S. Li, T. Chang, and J. Sun are with Science Systems and Applications Inc., Lanham, MD 20706, USA (e-mails: kevin.twedt@ssaihq.com, ning.lei@ssaihq.com, amit.angal@ssaihq.com,

xuexia.chen@ssaihq.com, junqiang.sun@ssaihq.com).

tiejun.chang@ssaihq.com,

X. Xiong is with Sciences and Exploration Directorate, NASA/GSFC, Greenbelt, MD 20771, USA (e-mail: xiaoxiong.xiong-1@nasa.gov)

TABLE I  
VIIRS RSB SPECIFICATIONS AND INITIAL MEASUREMENTS

Band	Center Wavelength	Bandwidth	Nadir spatial resolution (m)	Typical radiance	SNR Spec.	Measured SNR at Pre-launch	Measured SNR On-orbit	Measured Initial F-factor
I1	640	80	375	22	119	227	224	0.891
I2	865	39	375	25	150	287	282	0.901
I3	1610	60	375	7.3	6	190	178	1.060
M1 HG	412	20	750	44.9	352	636	641	0.855
M1 LG				155	316	1066	1110	0.878
M2 HG	445	18	750	40	380	573	566	0.887
M2 LG				146	409	986	1005	0.914
M3 HG	488	20	750	32	416	706	686	0.885
M3 LG				123	414	1063	1050	0.937
M4 HG	555	20	750	21	362	559	547	0.863
M4 LG				90	315	844	844	0.865
M5 HG	672	20	750	10	242	380	386	0.859
M5 LG				68	360	751	761	0.872
M6	746	15	750	9.6	199	428	415	0.885
M7 HG	885	39	750	6.4	215	549	527	0.884
M7 LG				33.4	340	760	709	0.901
M8	1240	20	750	5.4	74	335	322	0.993
M9	1378	15	750	6.0	83	325	297	1.053
M10	1610	60	750	7.3	342	765	660	1.082
M11	2250	50	750	1.0	90	216	199	1.053

The band center wavelength and bandwidth are in nm and the typical radiance ( $L_{typ}$ ) is given in  $Wm^{-2}sr^{-1}\mu m^{-1}$ . Note that all the specifications are the same for N20 VIIRS as they were for SNPP VIIRS, except for the band M11  $L_{typ}$  and SNR specifications. The SNR on-orbit measurement is an average over the first three years. The initial on-orbit F-factor is determined from the first day of SD measurements after instrument turn-on and temperature stabilization for the VIS/NIR bands and from the first day after cryocooler stabilization for the SWIR bands.

Libya 4 desert site. Special considerations for N20 calibration are discussed as well as possibilities for future improvements. Overall, the N20 RSB have had excellent early mission performance, with changes in gain of less than 0.5% in the first three years across all detectors, stable L1B reflectance, and stable values of detector SNR and reflectance uncertainty. Comparisons are also made to the first three years of operation of SNPP VIIRS. In most aspects, the N20 and SNPP VIIRS have similar on-orbit performance, but the N20 RSB have much more stable long-term gain trends compared to SNPP, due to the telescope mirror coating problem present for SNPP that was fixed for N20.

## II. VIIRS INSTRUMENT AND EARLY MISSION EVENTS

### A. VIIRS Design

The design and operation of the N20 VIIRS are nearly identical to the SNPP VIIRS. Figure 1 shows a schematic of the VIIRS instrument, including its on-board calibrators. A rotating telescope assembly (RTA) and half-angle mirror (HAM) together scan the VIIRS detectors over the Earth scene across the satellite track. The solar diffuser is the primary calibration source for the RSB, illuminated by the Sun once every orbit through a fixed attenuation screen. A solar diffuser stability monitor tracks the degradation of the SD by monitoring the ratio of the measured signal when viewing the SD to the measured signal when viewing the Sun through a separate solar attenuation screen. An on-board blackbody target is a calibration source for the TEB, and a space view (SV) port provides a deep space observation once every RTA scan for dark background subtraction.

The VIIRS RSB cover a wavelength range of 412 nm to 2250 nm. VIIRS acquires images at a nadir spatial resolutions of 750

m for the 11 moderate resolution “M” RSB and 375 m for the 3 imaging “I” RSB. A summary of the VIIRS RSB specifications and key design requirements is given in the first six columns of Table I. Six of the M bands (M1-M5, M7) are dual gain bands that can switch gain stage between low gain (LG) and high gain (HG) depending on the observed signal, to facilitate imaging of both bright and dark scenes with good SNR. When sampling the calibrator views (SD, blackbody, SV), the dual gain bands operate alternately in HG and LG stages to aid calibration of both stages. All VIIRS bands use pixel aggregation in the along-scan direction to reduce the impact of the pixel size growth toward the edges of the scan. At nadir, each EV pixel is the aggregation of 3 data samples, and the aggregation drops first to two data samples and then to one sample going from nadir to edge of scan.

### B. Early On-orbit Maneuvers and Events

During the first few months after launch, the N20 VIIRS went through an intensive series of post-launch calibration and

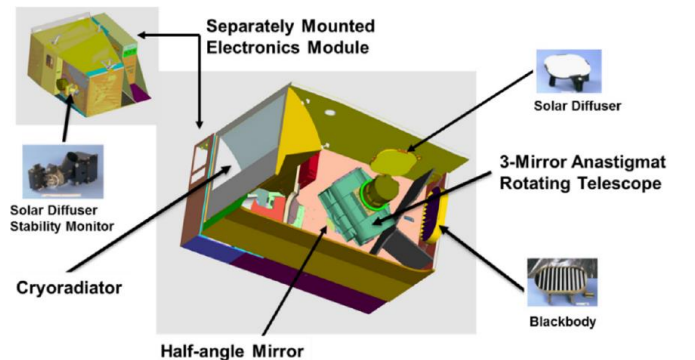


Fig. 1. A schematic of the VIIRS instrument.

TABLE II  
VIIRS RSB KEY EVENTS FOLLOWING NOAA-20 LAUNCH

Date	Event
November 18, 2017	NOAA-20 launch
November 28, 2017	VIIRS instrument activation
November 29, 2017	First SD calibration
November 30, 2017	First SDSM calibration
December 13, 2017	Nadir aperture door opened
December 29, 2017	First lunar observation
January 3, 2018	Cryo-radiator door opened
January 6, 2018	Cold focal plane temperatures stable
January 25-26, 2018	Yaw maneuvers
March 12-14, 2018	Mid-mission outgassing

testing [6], [7]. Table II lists key early mission events and maneuvers performed that are relevant to the reflective solar bands. The VIIRS instrument activation began on November 28, 2017, ten days after mission launch. VIIRS transitioned to science mode on November 29 and the VIIRS detectors began collecting data from the SD calibration events every orbit. The first calibration of the SDSM was performed on November 30, on the fourth orbit of SD observations. To facilitate optimal tracking of the early degradation of the SD, the SDSM was initially operated on every orbit. The operation frequency was later reduced to once per day on January 6, 2018 and to once per week on February 28, 2019 [13]. The first lunar observation occurred on December 29, 2017 and subsequent observations have been carried out every month when a suitable viewing geometry is available [16]. A set of spacecraft yaw maneuvers were performed on January 25-26, 2018. The SD and SDSM calibration data collected during these yaw maneuvers are used to derive on-orbit corrections to the SD and SDSM screen transmittance functions used in RSB calibration [17], [18].

The nadir aperture door was opened on December 13, 2017 and the VIIRS visible (VIS) and near infrared (NIR) bands began collecting Earth View (EV) imagery. On January 3, 2018, the cyro-radiator door was opened, allowing the cold focal planes to begin cooling. The temperatures stabilized a few days later and both calibration and Earth view data became available from the short-wave infrared (SWIR) detectors, as well as the TEB. After several weeks of cold focal plane operation, an unexpectedly large gain degradation was observed for a few LWIR TEB that was determined to be due to ice buildup on the cold focal plane dewar window. A mid-mission outgassing operation was performed from March 12-14, 2018 that successfully removed the ice buildup and restored stable gain trends for the TEB [14], [19]. The ice buildup and mid-mission outgassing did not have any significant impact on the RSB performance.

Additionally, the initial post-launch testing phase included several special calibrations to test other aspects of VIIRS performance, particularly for changes made to the DNB between SNPP and N20 [20]. Several analyses of N20 RSB have been presented by both VCST and groups at NOAA covering the initial post-launch calibration activities, showing stable and expected initial performance of the SDSM, SD, electronics, SNR, and RSB gains [6], [7], [21]–[23].

### III. RSB ON-ORBIT GAIN

The on-orbit F-factors (inverse gain) of the RSB detectors are determined using on-orbit observations of the SD. We recently reviewed the calibration algorithms used to generate both the SD degradation derived from SDSM measurements and also the F-factors derived from a combination of SD and lunar observations [13]. We review these algorithms briefly here.

The calibrated radiance of the VIIRS bands is defined as [8]

$$L_{EV} = F(c_0 + c_1 dn_{EV} + c_2 dn_{EV}^2 + c_3 dn_{EV}^3) / RVS_{EV}. \quad (1)$$

where  $c_{0,1,2,3}$  are pre-launch determined calibration coefficients which depend on the instrument temperature [24],  $RVS_{EV}$  is the pre-launch determined response versus scan angle, which is a function of the angle of incidence of light off the HAM, and  $F$  is the on-orbit determined overall change, inversely proportional to the instrument gain. For N20 VIIRS,  $c_0 = 0$  for all RSB and  $c_3 = 0$  for all RSB except the SWIR bands M8-M11, which showed larger non-linearity in pre-launch testing [25]. The reflectance factor product is defined as

$$\rho_{EV} \cos(\theta_{EV}) = \frac{4\pi^2 L_{EV} d_{sun}^2}{E_{sun}}. \quad (2)$$

where  $\theta_{EV}$  is the solar zenith angle,  $L_{EV}$  is from (1),  $E_{sun}$  is the solar spectral power integrated over the relative spectral response (RSR) function for each band, and  $d_{sun}$  is the VIIRS-Sun distance.

The F-factor is calculated from observations of the SD made once every orbit when the SD is illuminated by the Sun, calculated from (1) using the radiance of the SD:

$$F = \frac{RVS_{SD} \int RSR \Phi_{sun} \tau BRDF H_{RTA} \cos(\theta_{SD}) d\lambda}{4\pi d_{sun}^2 (c_0 + c_1 dn_{SD} + c_2 dn_{SD}^2 + c_3 dn_{SD}^3) \int RSR d\lambda}, \quad (3)$$

where  $RVS_{SD}$  is the RVS at the view angle of the SD,  $\Phi_{sun}$  is the solar spectral power as a function of wavelength,  $\tau$  is the SD screen transmittance,  $BRDF$  is the SD bi-directional reflectance distribution function at the start of the mission,  $\theta_{SD}$  is the angle between the solar vector and the SD surface normal,  $dn_{SD}$  is the detector signal when viewing the SD after background subtraction, and  $H_{RTA}$  is the H-factor from the view angle of the RTA (described below). The product of the screen transmittance and initial on-orbit BRDF is based on pre-launch measurements. We reviewed the angular dependence of this product using on-orbit measurements and found it to be reasonably accurate, so no on-orbit update has been made, though updates were made to the screen functions used in the SD degradation algorithms [17].

Of critical importance to obtaining an accurate  $F$  is the determination of the SD degradation,  $H_{RTA}$ . Measurements from the SDSM are used to track the on-orbit degradation of the SD, commonly referred to as the H-factor. The SDSM measures the SD degradation from the viewing direction of the SDSM at 8 different wavelengths from 410 nm to 930 nm. We define the H-factor measured directly by these 8 detectors as  $H_{measured}$ . After determining  $H_{measured}$  for each SDSM calibration, we

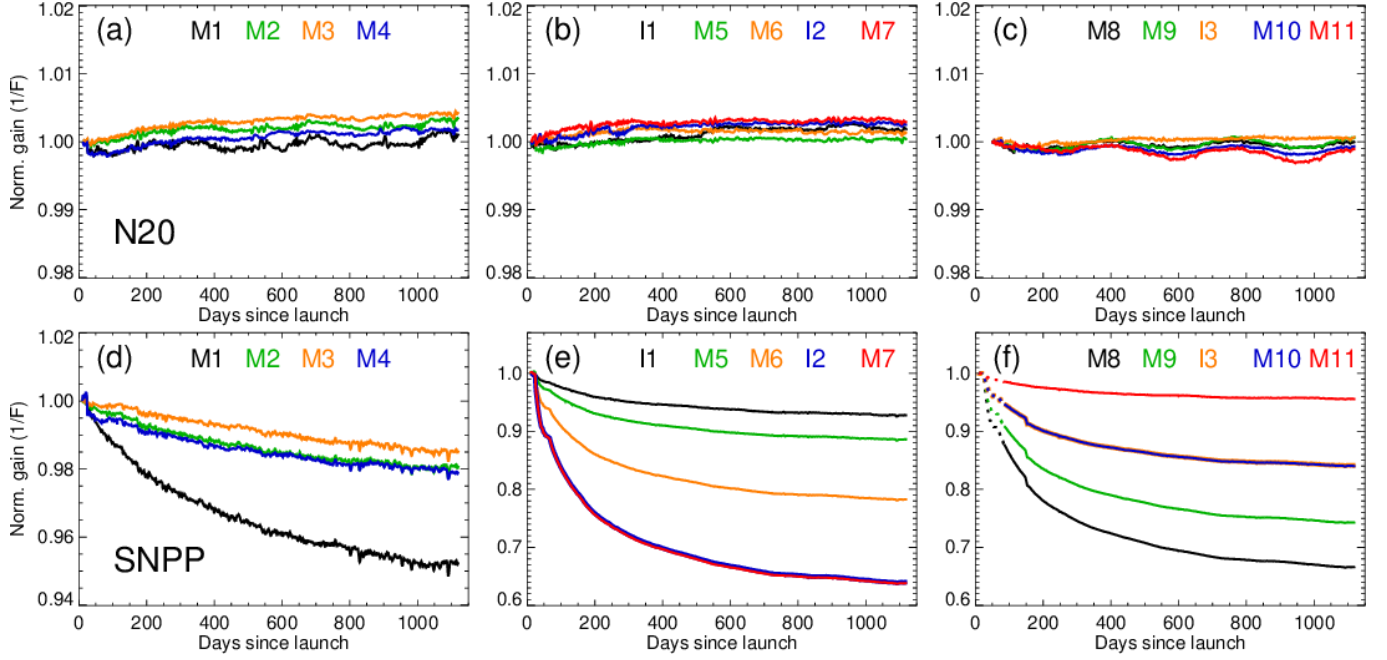


Fig. 2. On-orbit gain change ( $1/F$  normalized to mission start) for N20 (a-c) and SNPP (d-f) VIIRS for the first three years of each mission. For SNPP VIIRS SWIR bands (f), the dashed line near mission start represents the modeled gain degradation prior to the first measurements for these bands. Note the different vertical scales for SNPP compared to N20.

apply three additional corrections. The first is to remove the impact of the RSR of the SDSM detectors in order to derive the true H-factor as viewed from the SDSM direction. The second is to extrapolate the H-factors over the VIS/NIR wavelength range to the SWIR wavelengths (since the SDSM has no SWIR detectors) using a power-law fitting. These corrections combine to give  $H_{SDSM}$ , which is the SD degradation from the SDSM view direction interpolated to wavelengths of all VIIRS RSB.

Finally, we must apply an adjustment to convert the degradation at the SDSM view direction,  $H_{SDSM}$ , to the degradation at the view angle of the RTA,  $H_{RTA}$ , for use in calculating F from (3). Early in the SNPP VIIRS mission, it was found that the SD degradation has view angle dependence and it is not sufficient to calculate F using either  $H_{measured}$  or  $H_{SDSM}$  directly [26], [27]. The same result was found early in the mission for N20 VIIRS by investigating the SDSM response as a function of solar angle [28]. For SNPP VIIRS, a precise correction could be made by fitting the SD F-factor, calculated with  $H_{SDSM}$ , to the F-factors derived from lunar observations [27]. For N20 VIIRS, at the start of the NASA C2 L1B processing, there was insufficient lunar data (less than 2 years of observations) to use the N20 lunar data directly to derive a  $H_{SDSM}$ -to- $H_{RTA}$  correction. Instead, we use the fitting coefficients from the SNPP  $H_{SDSM}$ -to- $H_{RTA}$  correction, scale them down by a factor of approximately two based on the comparison of H-factor angular dependence from the SDSM studies, and apply them to the N20 VIIRS to derive the final  $H_{RTA}$ . We discuss comparisons to lunar data more in the Section IV. With the final  $H_{RTA}$ , we use (3) to calculate the F-factors.

Figure 2 shows the on-orbit trends of the gain ( $1/F$ ), normalized to the first on-orbit measurements for all RSB for the first 3 years of the N20 mission compared to the first three years of the SNPP mission. The trends are the average over all

detectors and both HAM sides for each band. For the dual gain bands, only the high gain stage is shown, though the low gain stage has very similar performance. The on-orbit performance of the N20 RSB has been extremely stable, with less than 0.5% change for any RSB detector. This is in sharp contrast to the SNPP gain changes in early mission, where the rapid degradation of the RTA mirrors caused the gain to drop more than 35% in the NIR wavelength range in the first three years [11].

Though the gain changes for N20 RSB are small, there are

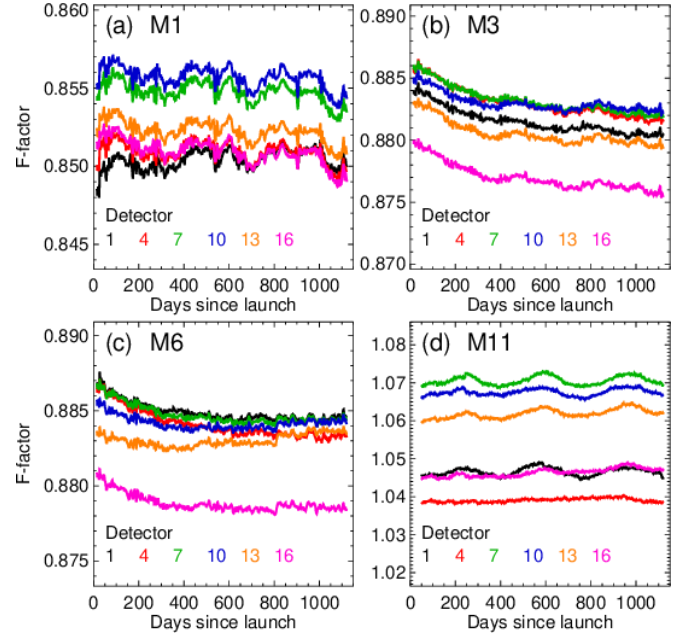


Fig. 3. F-factor trends for a few representative detectors in bands (a) M1, (b) M3, (c) M6, and (d) M11. Trends are for HAM side 1 and the high gain stage.

noticeable increases in the gain (decreases in  $F$ ) for all VIS and NIR bands. This is in the opposite direction of the typical expectation: that cumulative exposure to radiation in orbit degrades the instrument optics or other systems, leading to a decrease in gain. The observed gain increases could be the result of residual uncertainties in the calculation of  $H_{RTA}$  from scaled SNPP lunar fitting coefficients. This is a possibility for bands M1-M4, but less likely for the NIR bands, especially M6-M7 where the lunar-based correction is negligible. An increase in instrument gain is certainly possible, particularly at the small levels observed here. For example, both MODIS instruments have documented increases in their electronic subsystem gains of several percent over the missions [29].

None of the early mission events or maneuvers had any major impact on the RSB gains. A few SWIR band detectors had slight gain degradation, up to 0.15% for a few detectors in band M8, because of the ice build-up that mostly affected the LWIR TEB. The mid-mission outgassing completed on day 116 of the mission restored the performance, and the impact of this event is hardly noticeable in the band-average gain trends in Fig. 2.

The designation of the normalized gain as  $1/F$  is somewhat ambiguous due to the cubic form of the calibration function in (1). For example, the gain could alternatively be designated as  $1/(Fc_1)$ , which would include the temperature-dependent changes in gain that are included in the  $c_1$  coefficient. In practice though, the time-dependent trends of  $1/F$  and  $1/(Fc_1)$  are nearly identical, within 0.1% at all times for all RSB, so the choice of gain definition has no impact on the trends shown in Fig. 2.

Figure 3 shows the on-orbit  $F$ -factor trends for a few N20 RSB for different detectors within a band. Overall, all detectors within a band have very similar on-orbit trends, though the initial  $F$ -factor values in some cases can vary. In addition to the long-term stability, the  $F$ -factors also have very low short-term variation. The orbit-to-orbit and day-to-day variations in  $F$  are typically less than 0.1%, much less for some bands. In some cases, there can be seasonal variations in the  $F$  trends up to 0.2%, e.g. for band M1 in Fig. 3(a), which are possibly due to lingering inaccuracies in the angular dependence of the screen functions. The short-term  $F$ -factor variations for N20 RSB are similar to what has been observed for SNPP.

The initial, band-average, on-orbit values of the  $F$ -factors are listed in Table I. The values are significantly different from 1, which is an indication of discrepancies in the various pre-launch calibrations. The pre-launch calibration of the  $c$ -coefficients is based on an absolute radiometric calibration of the instrument's detectors using a lamp source of known radiance. On-orbit, the calibration is based on the solar radiance combined with the pre-launch measurements of the solar diffuser reflectance and screen transmittance. As designed, if the pre-launch measurements and the solar radiance LUTs are accurate, the  $F$ -factor at the time of launch should be close to 1 for all detectors. A deviation of the initial on-orbit  $F$ -factors from unity is either an indication of a discrepancy between the pre-launch radiance calibration and reflectance calibration, or an indication of a change in instrument or SD performance between pre-launch and on-orbit measurements. Ultimately, the pre-launch SD

measurements are the ones that are trusted to set the absolute scale for the on-orbit radiance and reflectance products. Comparisons to the reflectance of other instruments after the N20 launch (Section VI) indicates that the N20 on-orbit calibration (and by extension the pre-launch SD characterization) is accurate to within at least a few percent, and thus the large deviations seen in the at-launch  $F$ -factors are likely attributed mostly to errors in the pre-launch radiance calibration, though a reason for these errors is not fully understood.

We also note that the initial on-orbit  $F$ -factors for the VIS/NIR bands and the SWIR bands are very different: the VIS/NIR bands are all below 1 in the 0.85-0.90 range, whereas the SWIR bands are mostly greater than 1.0. This may be due to the different sources and/or optics used in the pre-launch calibration for the different wavelength ranges. For the VIS/NIR bands, the at-launch  $F$ -factor values are quite similar for all detectors within any given band, indicating that whatever caused the error in the pre-launch calibration was consistent across all detectors. For the SWIR bands M9, M10, and M11, there can be a few percent differences among detectors, as shown in Fig. 3, e.g. M11 compared to M6.



#### IV. LUNAR OBSERVATIONS

Regular lunar observations have been scheduled since launch for providing an independent calibration source for long-term radiometric stability monitoring of the VIIRS RSB. Nearly every month, a lunar calibration is performed to view the Moon around the phase angle of  $-51^\circ$  via a spacecraft roll maneuver to ensure that the Moon is viewed through the SV port. Through December 15, 2020, 23 lunar observations were performed for N20 VIIRS. The lunar calibration methodology employed for N20 VIIRS is similar to that developed for SNPP VIIRS with the exception of processing changes to account for the aggregation zone differences where the Moon is observed [16], [30].

The VIIRS measurement of the lunar radiance for each pixel is described by a polynomial expression of its detector response as follows:

$$L_{Moon} = F \cdot L_{Moon,PL} = F(c_0 + c_1 dn_{moon} + c_2 dn_{moon}^2 + c_3 dn_{moon}^3) / RVS_{SV}, \quad (4)$$

where the  $c_{0,1,2,3}$  are the same calibration coefficients as in (1),  $RVS_{SV}$  is the sensor response versus scan angle at the SV AOI, and  $dn_{Moon}$  is the background corrected detector response.  $F$  is the scaling factor for the on-orbit calibration coefficients and tracks the changes in the sensor response on-orbit. The lunar irradiance at VIIRS,  $I_{Moon,PL}$ , is calculated by integrating the radiance of the lunar pixels and then normalizing it with the model predicted lunar irradiance for that event. The  $I_{Moon,ROLO}$  is the USGS Robotic Lunar Observatory model (ROLO model) predicted lunar irradiance that depends on illumination and view geometry, including Moon-Sun distance, VIIRS-Moon distance, lunar phase angle and lunar librations [31].

Finally, a band-averaged F-factor derived from lunar calibration can be expressed as

$$F_{Moon} = \frac{I_{Moon,ROLO}}{I_{Moon,PL}}. \quad (5)$$

Figure 4(a-c) shows the gain ( $1/F_{Moon}$ ) of the VIIRS RSB computed from the scheduled lunar calibration plotted together with the daily-averaged gain derived from the SD measurements. To illustrate the long-term agreement of the SD and lunar data sets, the lunar gain trend (symbols) for each band is normalized to the SD gain trend using a single scaling factor determined from a least-squares fit. The SWIR bands were not operating at the nominal temperature until January 10, 2018 and therefore the first lunar measurement on December 29, 2017 has not been included for the SWIR bands. The SD and lunar-based gains for all bands show good agreement, within 0.5% and within the yearly variations in the lunar measurements.

Also plotted in Fig. 4 (d-f) is a comparison of the exact same lunar-derived gains to the SD gains when the SD F-factor is calculated using  $H_{measured}$  instead of  $H_{RTA}$ . In this case, there is a clear divergence between the SD and lunar gains for the visible wavelength bands, up to about 1.8% for band M1 after three years. The divergence between SD gain (with  $H_{measured}$ ) and lunar gain is similar to the divergence reported in independent calibration done by NOAA [12]. Remember that the SD gain (with  $H_{RTA}$ ) in Fig. 4(a-c) is calculated without using any of the N20 lunar data and instead uses scaled results from SNPP VIIRS. The excellent agreement with the N20 lunar data confirms that the algorithm described in Section III and in [13] performs well and could also be extended to the early mission calibration of future VIIRS instruments. Now that more than three years of observations are available, we plan to investigate using the N20 lunar data directly to derive the  $H_{SDSM}$ -to- $H_{RTA}$  corrections in future calibration updates.

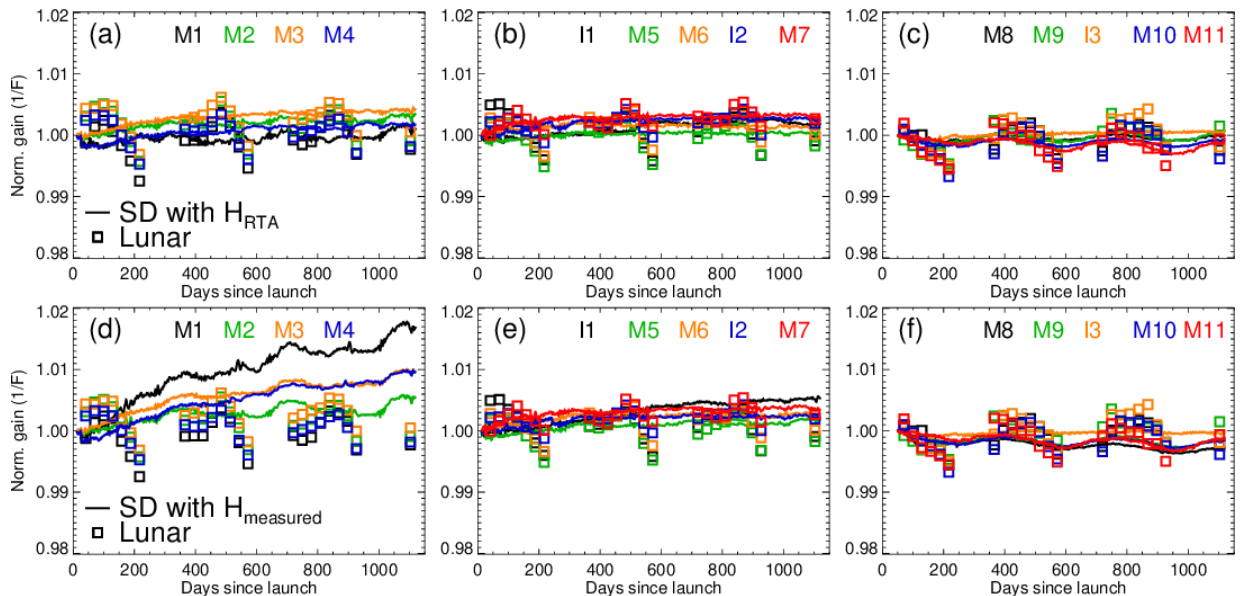


Fig. 4. (a-c) Band-average on-orbit changes in gain ( $1/F$ ) for the (a) VIS, (b) NIR, and (c) SWIR bands. The SD gains (solid lines) are shown for all RSB normalized to the value at the start of the mission. Only the high gain stage of the dual gain bands is shown. The lunar gains (symbols) for each band are scaled to the SD gains using a single scaling factor determined from a least-squares minimization. (d-f) SD gains calculated using  $H_{measured}$  instead of  $H_{RTA}$  compared to the same lunar data.

## V. ON-ORBIT UNCERTAINTY ASSESSMENTS

### A. Noise and SNR

In addition to accurate tracking of the instrument gain, the quality of the Earth reflectance measurements depends on having accurate knowledge of the uncertainties in the measurement, both from statistical instrument noise and from any potential biases in the pre-launch or on-orbit calibration methods. In this section, we first review the instrument noise performance and the SNR at typical radiance levels, and then we discuss the on-orbit reflectance uncertainty.

The methodology for calculating and tracking the on-orbit noise and SNR performance of the VIIRS RSB was presented previously for SNPP [11], [32]. We use the same methodology for N20 VIIRS. For a single EV pixel, the variance in the value of the retrieved signal,  $dn_{EV}$ , that is due solely to the instrument noise follows

$$\sigma_{EV}^2 = k_0 + k_1 dn_{EV}, \quad (6)$$

where  $k_0$  and  $k_1$  are time-dependent coefficients. This is slightly different than the way the noise is defined for pre-launch measurements [24], but similar to conventions used for on-orbit noise characterization of other remote sensing instruments. The constant term in (6) represents the zero radiance noise which can include thermal, electronic, and digitization noise, and the linear term represents the photon noise which increases with signal strength (radiance).

The coefficients  $k_0$  and  $k_1$  are determined from the every-orbit solar diffuser observations. For each scan of the HAM, 48 samples of data are collected while the RSB detectors are viewing the SD (96 samples for the I bands). Assuming the SD radiance is perfectly stable across the samples, the variance in the signal can be attributed solely to instrument noise. The variance in  $dn_{SD}$  is expressed as  $\sigma_{SD}^2$  and is calculated for every scan where the SD is either fully or partially illuminated by the Sun. Collecting data over a range of solar illumination/radiance levels allows for tracking of the signal dependence of the noise. Note that the variance in the subtraction of the average background signal is already included in  $\sigma_{SD}$  and is equivalently included in  $\sigma_{EV}$ . However, the noise in the single-pixel SD measurement cannot be directly equated to the noise in the single-pixel EV measurement due to a difference in quantization error. For VIIRS, the analog instrument signal is truncated to 14-bits for the SD sector data and to 12-bits for the EV sector data onboard the instrument before the data is transmitted. As a result, the EV sector data has a higher digitization error, which can be expressed as [32]

$$\sigma_{EV}^2 = \sigma_{SD}^2 + \frac{1}{12} - \frac{1}{192}. \quad (7)$$

With the quantization-corrected values of variance for each scan, the values are fit to a linear function of  $dn_{SD}$  to derive the  $k_0$  and  $k_1$  coefficients. The values can be calculated for each SD calibration (every orbit) to track their change in time.

With the noise determined, the SNR can be calculated from

$$SNR_{typ} = dn_{typ} / \sqrt{k_0 + k_1 dn_{typ}}, \quad (8)$$

where the  $dn_{typ}$  is determined from the specified typical radiance  $L_{typ}$  (Table I) using the radiance equation and the F-factor at the given point in time:

$$L_{typ} = F(c_0 + c_1 dn_{typ} + c_2 dn_{typ}^2 + c_3 dn_{typ}^3). \quad (9)$$

Figure 5 shows trends of the noise coefficients  $k_0$  and  $k_1$  and the SNR at typical radiance for two example detectors: band I2 detector 16 and band M1 detector 8 in the high gain stage. Also shown in Fig. 5 are the same quantities for SNPP VIIRS over the first three years of the SNPP mission. The noise coefficients for both VIIRS instruments are very stable on orbit. Overall, the zero signal noise  $k_0$  is somewhat lower for N20 compared to SNPP, by a varying amount per band, and  $k_1$  is similar for both instruments across all bands and detectors. For the SNR at typical radiance, the values for N20 are very stable on orbit for all detectors. For SNPP, the SNR at mission beginning is very similar to N20 VIIRS, but the SNR decreases on orbit due to the decrease in instrument gain that is most significant in the NIR wavelengths, such as band I2 shown in Fig. 5. The SNR at typical radiance for N20 VIIRS RSB detectors is well above the SNR specification, as shown in Fig. 6, and very consistent among all detectors within a band. The average of on-orbit SNR at typical radiance over the first three years of N20 mission are also listed in Table I. The on-orbit numbers are consistent with the pre-launch measurements despite the differences in characterization source and methodology.

All N20 RSB detectors remain operable, and only one detector is listed as noisy. Detector 29 of band I3 had large noise and out-of-family gain in pre-launch characterization and continues to have poor performance on-orbit. The F-factor for this detector has been around 2 for most of the mission, with significantly higher noise than the other I3 detectors. The SNR for this detector is between 2 and 3. The detector continues to be calibrated but is flagged as noisy in the C2 L1B products. The values of band-average I3 SNR and initial F-factor in Table

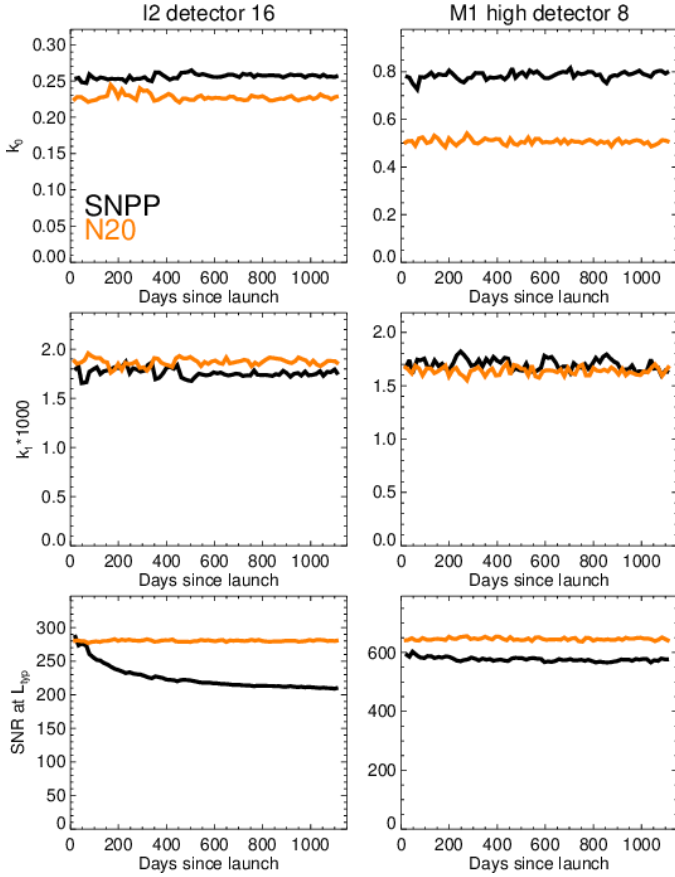


Fig. 5. On-orbit trends of  $k_0$ ,  $k_1$ , and SNR at typical radiance for N20 compared to SNPP VIIRS for one example detector of band I2 and band M1 high gain.

I have this noisy detector excluded.

### B. Reflectance Uncertainty

The specified uncertainty requirement for the VIIRS RSB is that the reflectance uncertainty be less than 2% for scenes at the specified typical radiance. Some uncertainty analyses were conducted during pre-launch testing based on component-level measurements. Here, we focus mainly on the on-orbit components of the uncertainty that can change in time. The uncertainty in the L1B reflectance product,  $\rho_{EV} \cos(\theta_{EV})$  from Eq. 2, for N20 VIIRS can be derived from the calibration parameters in a similar way as we have previously shown for SNPP VIIRS [11], [33]. The total relative uncertainty in the Earth view reflectance factor is calculated from

$$\left[ \frac{\text{var}(\rho_{EV} \cos(\theta_{Earth-Sun}))}{\rho_{EV}^2 \cos^2(\theta_{Earth-Sun})} \right]^{1/2} = \left[ \frac{\text{var}(H_{RTA})}{H_{RTA}^2} + \frac{\text{var}(dn_{EV})}{dn_{EV}^2} + \frac{\text{var}(\tau_{SD} \text{BRDF}_{RTA}(t=0))}{[\tau_{SD} \text{BRDF}_{RTA}(t=0)]^2} \right]^{1/2}, \quad (10)$$

where  $\text{var}()$  indicates the variance of the enclosed quantity. In deriving (10) from (2), we have assumed that the relative uncertainty contributions from several of the terms are small, including the VIIRS-Sun distance, RVS,  $\theta_{SD-Sun}$ , and the pre-launch c-coefficients. The three terms on the right-hand side of (10) are the dominant contributors to the overall uncertainty.

The uncertainty in  $H_{RTA}$  was derived in detail in our previous

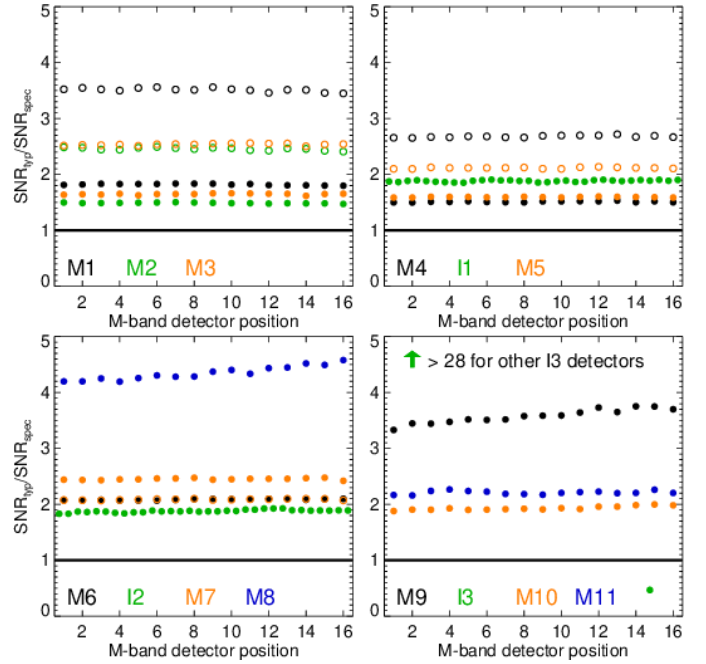


Fig. 6. SNR at typical radiance divided by the specification SNR (see Table I) for each RSB detector, including high gain (filled circles) and low gain (open circles) stages for the dual gain bands. Detector values are plotted as a function of M-band position, with two I-band detectors per M-band detector. Values are the average over the first three years of on-orbit measurements. The  $SNR_{typ}/SNR_{spec}$  values for I3 detectors are between 28 and 30, well above the scale of the plot, with the exception of noisy detector 29. The values for M6 and M7 low gain are very similar, causing the symbols to overlap in the plot.

N20 SD calibration paper [13]. The values for all RSB were estimated at around 0.1% near the beginning of the mission. The uncertainty increases slightly over the mission due to the increasing SD degradation, with a larger increase for shorter wavelength bands, but even in the worst case (band M1) the  $H_{RTA}$  uncertainty was estimated to be less than 0.2% after three years on orbit.

The second term on the right side of (10) accounts for the pixel-level noise in the EV signal and depends on the radiance of the observed scene. Here, the value of  $\text{var}(dn_{EV})$  depends on the aggregation of the EV pixel. For pixels near the beginning and end of scan where there is no pixel aggregation, the variance is the single pixel variance as defined in (6),  $\text{var}(dn_{EV}) = \sigma_{EV}^2$ . Moving toward the center of scan, the EV pixels in the L1B product are the aggregation of 2 and then 3 individually measured samples. The variance of the aggregated pixel can be conceptually thought of as the single-pixel variance divided by the number of aggregated pixels, i.e.  $\text{var}(dn_{EV}) = \sigma_{EV}^2/2$  for the 2-pixel aggregation zones and  $\text{var}(dn_{EV}) = \sigma_{EV}^2/3$  for the 3-pixel aggregation zone (near-nadir pixels). This is roughly accurate, but the precise calculation is slightly different due to differences in how the aggregation and digitization are handled for single gain and dual gain bands [11], [32]. Importantly, the pixel aggregation further reduces the noise such that the pixel-to-pixel SNR for near-nadir pixels is even higher than the single-sample SNR numbers reported in Section V-A.

The third term on the right side of (10) represents the uncertainty in the initial at-launch values of the SD reflectance



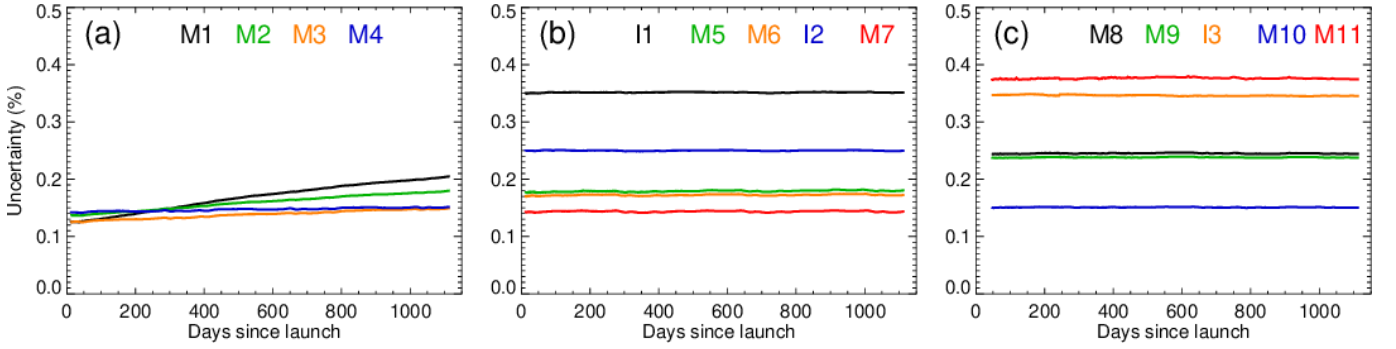


Fig. 7. Reflectance uncertainty for on-orbit uncertainty terms as a function of time since launch for each of the VIIRS RSB, averaged over all non-noisy detectors in a band, evaluated at typical radiance levels and at nadir view. For the dual gain bands, only the high gain stage is shown.

and the SD screen transmittance. The estimated uncertainty in the pre-launch calibration of the SD BRDF was reported to be 0.76% over most of the RSB wavelength range [34]. However, this included only the uncertainty in SD reflectance measurements and does not include the SD screen transmittance uncertainty or any other systematic biases that might contribute to the at-launch SD BRDF uncertainty, such as changes in the SD BRDF from pre-launch measurement to first on-orbit measurement, the impact of stray light on the SD surface, etc. A full accounting of the uncertainties in the pre-launch measurements related to the SD reflectance as well as smaller uncertainties from pre-launch measurements of RVS and  $c$ -coefficients has not been presented before and this is reserved for future work. Here we focus on the on-orbit uncertainty contributions which can change in time.

Figure 7 shows the time dependence of the on-orbit contributions to the uncertainty in the reflectance factor after combining the uncertainties of the  $H_{RTA}$  and the pixel noise. For band M1-M4, there is a slight increase in uncertainty over time due to the increase in uncertainty of  $H_{RTA}$ , but for all other bands the uncertainty is very stable on-orbit. Across all RSB, the values fall between 0.1% and 0.4%. Figure 7 shows the uncertainty for the high gain stage only of the dual gain bands. The low gain stage values are somewhat different, due to different values of SNR, but all fall within the same general

range.

The uncertainty in Fig. 7 is evaluated at typical radiance levels and at nadir view. As discussed, the uncertainty is lower at nadir and higher toward the edges of scan due to the differences in pixel aggregation. The uncertainty is also higher for lower radiance levels. To demonstrate, Fig. 8 shows an example of how the uncertainty can vary across a single Earth view scan. Values are shown for M5 high gain stage at typical radiance and at 0.3 times the typical radiance. Even at the lower radiance level and toward the edge of the scan, the on-orbit uncertainty is still only 0.7% or less. At radiance levels larger than  $L_{typical}$ , the uncertainty is even smaller than the values shown in Fig. 7 and Fig. 8.

The small and stable values of on-orbit uncertainty in Figs. 7 and 8 indicate that the total uncertainty in N20 VIIRS RSB reflectance is likely dominated by the uncertainty in at-launch SD BRDF. Based on pre-launch measurements, this value will be 0.76% at a minimum and likely larger once all pre-launch measurement uncertainties are fully taken into account. Of course, it is also possible that unknown systematic biases existed in the measurements which can cause the absolute calibration to be off by more than the pre-launch uncertainty estimates would indicate. This is considered in Section VI when discussing the observed reflectance differences between N20 and SNPP VIIRS. Regardless of the absolute accuracy, the on-orbit RSB performance for N20 is clearly very stable and there is very little uncertainty in the on-orbit reflectance trends. In future work, we will investigate providing a pixel-level uncertainty index in the L1B product, similar to what is currently available in the MODIS L1B [35].

## VI. REFLECTANCE PERFORMANCE ASSESSMENTS

### A. L1B reflectance product

The NASA N20 C2 L1B reflectance product has been in production since about August 2019. VCST delivered the first set of look-up-tables (LUTs) for the F-factor in mid-2019 and has updated these regularly since then. All other LUTs relevant to the RSB are fixed values from pre-launch measurements and are also consistent with the LUTs used in generation of NOAA SDR products [12].

The F-factor LUTs used in the L1B are determined from empirical fits to the measured SD F-factors shown in Fig. 2(a-c). In the initial delivery in mid-2019, the measured F were fit

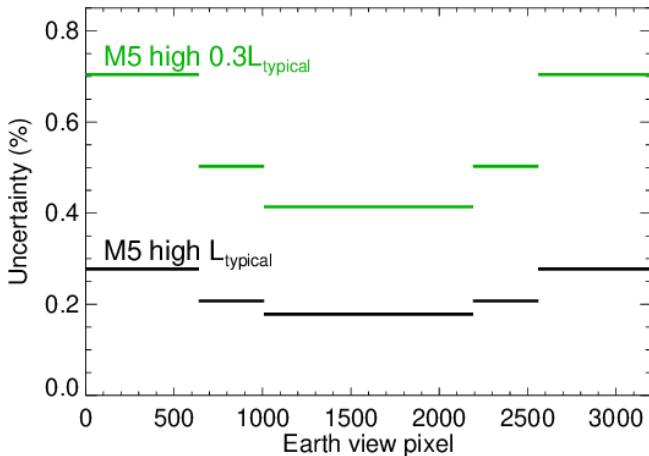


Fig. 8. Example of uncertainty variation as a function of Earth view pixel location within one scan for two different radiance levels:  $L_{typical}$  and  $0.3L_{typical}$  for band M5 high gain.

to a sliding 3-week quadratic fit, so that the F LUTs largely follow the up and down undulations in the data that can be up to a few tenths of a percent, as seen for individual detectors in Fig. 3. After the first delivery, the F LUTs used in C2 production are forward predicted LUTs and are updated as needed. Initially, forward updates were made frequently (once every four to six weeks) to attempt to continue to follow the short-term undulations in the measured F. More recently, around July 2020, the forward prediction scheme was changed. Currently, the most recent 1.5 years of measured F are fit to a linear function to generate a prediction to the forward F. Due to the continued stable performance of the measured F, the predicted F LUTs are nearly flat in time and they are updated much less frequently (once every six months), though they do not follow the small short-term undulations in the measured F. The F LUTs used for N20 C2 production agree to within  $\pm 0.2\%$  with the measured F-factor values at any point in time for all detectors, and much closer in many cases.

### B. L1B reflectance trends

We routinely monitor the performance of NASA's N20 C2 L1B reflectance product using stable Earth calibration targets. Figure 9 shows the normalized reflectance trends from the widely used Libya 4 desert site ( $+28.55^\circ$ ,  $+23.39^\circ$ ) near nadir for most N20 VIIRS RSB. The C2 reflectance is averaged over a 32 by 32 pixel area (about 576 km<sup>2</sup>) and all detectors and both mirror sides are averaged together. Each observation in Fig. 9 is taken from a consistent viewing angle about 83 km from nadir. A kernel-driven empirical BRDF model [36] is applied to remove seasonal oscillations and then the trends are normalized to the average of the first two years values from mission beginning. Bands M6, M9, and M11 are not included in Fig. 9 due to saturation, large atmospheric absorption, and low signal, respectively, when viewing the Libya 4 site. The reflectance trend for I3, not shown for brevity, is very similar to the spectrally matched M10.

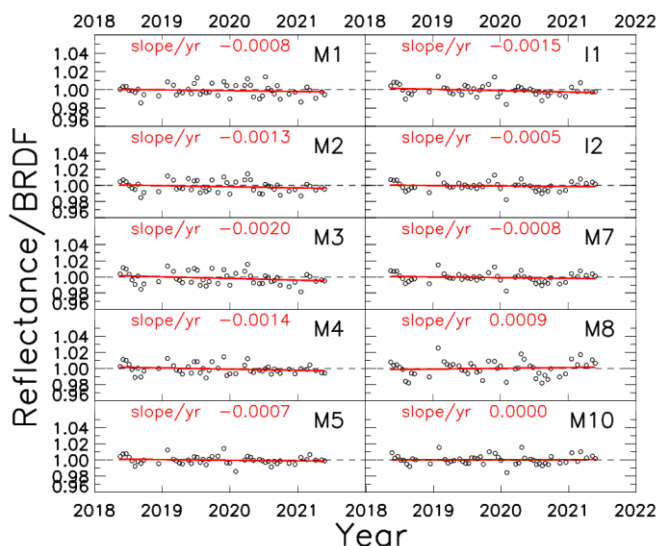


Fig. 9. Normalized reflectance trends from Libya 4 site near nadir for select RSB. Black points are individual observations and red lines are linear fits over the entire times series. The slopes of the linear trends in relative reflectance change per year are printed in red text in each panel.

For all bands, the reflectance trends are stable over the first three years of the mission. Linear fits of the measurements over the entire mission so far show reflectance drifts of less than 0.2% per year for all bands. While the magnitudes of these trends are within the measurement noise, the trends are consistently downward for all VIS/NIR bands. As shown in Section III, the F-factors for the VIS/NIR bands all trend slightly downward (gains trend upward). The slight downward trends in the Libya 4 reflectance may indicate that these slight downward trends in F are not real, but the uncertainty in the desert measurements is too large for this to be conclusive. We also routinely monitor N20 RSB reflectance trends from deep convective clouds (DCC), similar to what our group has previously published for SNPP VIIRS RSB [37], and also find stable reflectance trends for all bands to within the measurement noise. The observations in Fig. 9 are from only one viewing angle near nadir. Further analysis of the reflectance trends from both desert sites and DCC at multiple viewing angles can be used to assess the reflectance performance across the entire scan range and evaluate the on-orbit stability of the RVS. These analyses are in progress in our group and the results are reserved for future work. Continued observations of these stable sites will be necessary to ensure the calibration continues to perform well on multi-year timescales.

In addition to the band-average reflectance stability, we have also used the Libya 4 site to check the relative accuracy of the reflectance between detectors and mirror sides within a band [38]. This study found no significant evidence of image striping in bands M1-M7, with all detector differences within  $\pm 0.3\%$  or less of the band average. Larger detector differences were seen for the SWIR bands M8, M10, and M11, up to  $\pm 1\%$  away from the band-average, which may be related to the known non-linear gain concerns in these bands. The HAM-side reflectance differences were also investigated and found to be very small with the exception of band M1, which showed HAM side 1 to have about 0.5% lower reflectance than HAM side 2 consistently across detectors. This HAM-side difference was also observed in the lunar radiance [16]. The results indicate a slight HAM side dependent error in SD calibration, but the reason is not currently known. Both the observed detector differences in SWIR band reflectance and the HAM-side differences in M1 reflectance are stable in time over the first three years.

### C. Intercomparison

An essential part of evaluating the performance of a remote sensing instrument is comparing the absolute reflectance and radiance measurements with absolute measurements from other sensors, whether they be space-based or ground-based. We regularly track comparisons between N20 and SNPP VIIRS L1B reflectance using various Earth targets, including simultaneous nadir overpasses, pseudo-invariant Saharan desert and Antarctic snow sites, and DCC, and have recently reported these results [11], [39]. Generally, we found that N20 VIIRS has significantly lower reflectance than SNPP VIIRS for most RSB. The differences are larger at shorter wavelengths, roughly 3% to 6% for the VIS/NIR bands and 2% to 3% for the SWIR

bands. Through the same analyses, we found the reflectance of Aqua MODIS to be between that of the two VIIRS instruments.

The N20-SNPP comparison results are stable in time through the first three years of N20 mission, indicating a static calibration error. The source of the calibration error is not known but is likely related to differences in the pre-launch calibration of the SD reflectance between the two VIIRS instruments. The relatively large discrepancy poses a challenge for integrating the results of both sensors in the downstream science and environmental data products, which will involve the derivation and application of adjustment factors [40].

N20-SNPP reflectance comparisons have also been performed by using the NOAA Sensor Data Record products. These products use the same pre-launch calibration results as the NASA L1B products but are calibrated independently on-orbit. The N20-SNPP reflectance differences also exist in the NOAA products [12], [41], [42], though the magnitude of the differences are slightly different than in the NASA products due mostly to differences in the SNPP on-orbit calibration.

## VII. SPECIAL CONSIDERATIONS

While the on-orbit performance of the RSB has been excellent, there have been a few concerns identified with instrument performance that can affect the quality of the L1B and science products. The most notable concerns from pre-launch testing were the polarization sensitivity of the short wavelength VIS bands and the non-linear gain of the SWIR bands. Pre-launch measurements of the degree of linear polarization (DOLP) found bands M1-M4 to be above the design requirements (2.5% - 3% depending on band) and about a factor of two larger than the corresponding values for SNPP VIIRS. The largest DOLP was for band M1, up to 6%, varying with detector position and scan angle [43], [44]. The larger polarization sensitivity was found to have a significant impact on ocean scene radiance measurements on-orbit, and scene-dependent corrections may be needed to improve the image quality and accuracy [45].

Also during pre-launch testing, the SWIR bands M8-M11 were observed to have significant non-linear gains. Though all other bands use a quadratic polynomial to characterize the relationship between the radiance and detector signal, there were large residuals in the fitting of the pre-launch measurements when using a quadratic, or even a cubic, polynomial for M8-M11 [25]. A study using solar eclipse events to validate detector linearity on-orbit found that the non-linear behavior of these bands likely persists on-orbit [46]. As a result, there may be more signal-dependent impact on the Earth reflectance products for these bands compared to SNPP VIIRS and to other N20 RSB, though the absolute impact is not expected to be large.

Unlike SNPP VIIRS, the N20 VIIRS RSB continue to use the pre-launch measured relative spectral response (RSR) LUTs in calculation of the F-factor and L1B reflectance product. SNPP had multiple on-orbit updates to its RSR LUTs in the first few years of its mission to account for changes caused by the rapid optics degradation in the NIR wavelength range. For N20 VIIRS, the performance has been much more stable and the magnitude of the out-of-band components of RSR is also much

smaller than for SNPP VIIRS [24], [47], so no updates have been required.

The higher-resolution I bands have twice as many detectors as the M bands along-track and also record twice as many samples along scan: two sub-samples for every M-band sample. In principle, the data from the two sub-samples can be separated in the SD calibration and the F-factors determined separately. The current F-factor LUTs used in the L1B are specified per band, detector, gain stage, and HAM side, but are not separated by sub-sample for the I bands. We have found the sub-sample differences in the SD calibration to be relatively small, at most 0.4% for band I2 and much smaller for bands I1 and I3 [48]. Adding sub-sample dependence to the F LUT can be considered for future L1B versions, but the impact is expected to be minor, especially near nadir where the aggregation helps to smooth out any sub-sample differences.

In July 2020, an update was made to the pre-launch RVS values used in N20 VIIRS calibration, both to the RVS LUT used in generating EV reflectance values, and to the RVS values used in calculating the SD F-factors. The update was made to correct a slight error in the initial pre-launch RVS tables, but the RVS remains constant on-orbit, with no evidence of any change seen in the Earth view data. While the RVS update had a modest impact for some of the thermal emissive bands, the impact on RSB calibrated reflectance was very small, generally within 0.1%. The N20 Collection 2 L1B (Archive Set 5200) uses the updated RVS LUT in forward production starting from August 2020. The N20 Collection 2.1 L1B (Archive Set 5201) uses the updated RVS for the entire mission and is expected to be released in mid-2021. The RSB calibration methodology for C2 and C2.1 is identical, except for the minor change in RVS.

## VIII. SUMMARY

In the first three years of on-orbit operation the VIIRS instrument on the NOAA-20 satellite has had very stable performance. The total system gains of the reflective solar band detectors have changed by less than 0.5%. The N20 VIIRS RSB gains are much more stable compared to SNPP VIIRS in the first three years of each mission, due to the lack of RTA mirror contamination. The RSB calibration algorithms developed by VCST are used to calculate F-factor LUTs for the generation of NASA L1B reflectance product for N20 Collections 2 and 2.1. The algorithm using scaled values of lunar-SD fitting coefficients from SNPP is shown to give accurate calibration of N20 RSB for early mission times when there was only limited N20 lunar data available. The same algorithm can be extended to early mission calibration of future VIIRS missions.

The single pixel noise is stable and the SNR at typical radiance is at least 40% above specification for all bands. The on-orbit contributions to reflectance uncertainty at nadir and typical radiance are less than 0.5%, though a potentially large bias may exist in the pre-launch calibration. Comparisons of L1B reflectance with SNPP VIIRS have found differences of 3% to 6% for the VIS/NIR bands and 2% to 3% for the SWIR bands and more work is needed to better understand the source of these differences and mitigate their impact on science products. The performance of the C2 L1B reflectance has been stable in time, as evaluated using lunar observations and pseudo-invariant homogenous Earth targets. Striping in EV

imagery is very small for most bands, with some minor impacts up to 0.5% for M1 and up to 1% for some SWIR bands. Future work will focus on including N20 lunar data directly in the calibration, development of a complete uncertainty analysis and L1B uncertainty index, and investigation of potential calibration improvements to address polarization sensitivity, non-linear gain, and other minor calibration concerns.

#### ACKNOWLEDGMENT

We thank other past and present members of the NASA VIIRS Characterization Support Team for their work on N20 pre-launch and post-launch testing, and on-orbit calibration. We also thank Daniel Link for providing a review of this paper and many thoughtful comments.

#### REFERENCES

- [1] G. Lin, R. E. Wolfe, J. C. Tilton, P. Zhang, J. Dellomo, and B. Tan, "JPSS-1/NOAA-20 VIIRS early on-orbit geometric performance," in *Proceedings of SPIE*, Sep. 2018, vol. 10764, p. 107641H. doi: 10.1117/12.2320767.
- [2] "VIIRS Radiometric Calibration Algorithm Theoretical Basis Document." [Online]. Available: <https://ncc.nesdis.noaa.gov/VIIRS/VIIRSCalATBD.php>
- [3] C. F. Schueler, J. E. Clement, P. E. Ardanuy, C. Welsch, F. DeLuccia, and H. Swenson, "NPOESS VIIRS sensor design overview," in *Proceedings of SPIE*, Jan. 2002, vol. 4483, pp. 11–23. doi: 10.1117/12.453451.
- [4] P. E. Ardanuy *et al.*, "NPOESS VIIRS design process," in *Proceedings of SPIE*, Jan. 2002, vol. 4483, pp. 24–34. doi: 10.1117/12.453461.
- [5] R. E. Murphy, P. Ardanuy, F. J. DeLuccia, J. E. Clement, and C. F. Schueler, "The Visible Infrared Imaging Radiometer Suite," in *Earth Science Satellite Remote Sensing*, J. J. Qu, W. Gao, M. Kafatos, R. E. Murphy, and V. V. Salomonson, Eds. Berlin, Heidelberg: Springer Berlin Heidelberg, 2006, pp. 199–223. doi: 10.1007/978-3-540-37293-6\_11.
- [6] C. Cao *et al.*, "NOAA-20 VIIRS on-orbit performance, data quality, and operational Cal/Val support," in *Proceedings of SPIE*, Nov. 2018, vol. 10781, p. 107810K. doi: 10.1117/12.2324329.
- [7] X. Xiong, H. Oudrari, J. McIntire, N. Lei, V. Chiang, and A. Angal, "Initial calibration activities and performance assessments of NOAA-20 VIIRS," in *Proceedings of SPIE*, Oct. 2018, vol. 10781, p. 107810L. doi: 10.1117/12.2326897.
- [8] X. Xiong *et al.*, "VIIRS on-orbit calibration methodology and performance," *J. Geophys. Res. Atmospheres*, vol. 119, no. 9, pp. 5065–5078, May 2014, doi: 10.1002/2013JD020423.
- [9] T. Choi, X. Shao, and C. Cao, "On-orbit radiometric calibration of Suomi NPP VIIRS reflective solar bands using the Moon and solar diffuser," *Appl. Opt.*, vol. 57, no. 32, p. 9533, Nov. 2018, doi: 10.1364/AO.57.009533.
- [10] R. E. Eplee, K. R. Turpie, G. Meister, F. S. Patt, B. A. Franz, and S. W. Bailey, "On-orbit calibration of the Suomi National Polar-Orbiting Partnership Visible Infrared Imaging Radiometer Suite for ocean color applications," *Appl. Opt.*, vol. 54, no. 8, p. 1984, Mar. 2015, doi: 10.1364/AO.54.001984.
- [11] N. Lei, X. Xiong, Z. Wang, S. Li, and K. Twedt, "SNPP VIIRS RSB on-orbit radiometric calibration algorithms Version 2.0 and the performances, part 2: the performances," *J. Appl. Remote Sens.*, vol. 14, no. 04, Oct. 2020, doi: 10.1117/1.JRS.14.047502.
- [12] T. Choi, C. Cao, S. Blonski, W. Wang, S. Uprety, and X. Shao, "NOAA-20 VIIRS Reflective Solar Band Postlaunch Calibration Updates Two Years In-Orbit," *IEEE Trans. Geosci. Remote Sens.*, vol. 58, no. 11, pp. 7633–7642, 2020, doi: 10.1109/TGRS.2020.2982764.
- [13] N. Lei, K. A. Twedt, X. Xiong, and A. Angal, "Performance of NOAA-20 VIIRS Solar Diffuser and Solar Diffuser Stability Monitor," *IEEE Trans. Geosci. Remote Sens.*, pp. 1–9, 2020, doi: 10.1109/TGRS.2020.3032068.
- [14] Y. Li, X. Xiong, J. McIntire, A. Angal, S. Gusev, and K. Chiang, "Early Calibration and Performance Assessments of NOAA-20 VIIRS Thermal Emissive Bands," *IEEE Trans. Geosci. Remote Sens.*, vol. 57, no. 11, pp. 9242–9251, Nov. 2019, doi: 10.1109/TGRS.2019.2925782.
- [15] H. Chen, X. Xiong, D. O. Link, C. Sun, and K. Chiang, "NOAA-20 Visible Infrared Imaging Radiometer Suite day–night band on-orbit calibration and performance," *J. Appl. Remote Sens.*, vol. 14, no. 03, Sep. 2020, doi: 10.1117/1.JRS.14.034516.
- [16] A. Angal, X. Xiong, T. M. Wilson, X. Geng, and H. Chen, "Lunar calibration and performance assessments of the NOAA-20 VIIRS reflective solar bands," in *Proceedings of SPIE*, Sep. 2019, vol. 11127, p. 111272B. doi: 10.1117/12.2530024.
- [17] N. Lei and X. Xiong, "Determination of the NOAA-20 VIIRS screen transmittance functions with both the yaw maneuver and regular on-orbit calibration data," *Appl. Opt.*, vol. 59, no. 10, p. 2992, Apr. 2020, doi: 10.1364/AO.386979.
- [18] T. Choi, X. Shao, S. Blonski, and C. Cao, "On-orbit NOAA-20 VIIRS solar diffuser bidirectional reflectance distribution function and screen transmittance characterization using yaw manoeuvres and regular on-orbit SDSM data," *Int. J. Remote Sens.*, vol. 41, no. 17, pp. 6503–6526, Sep. 2020, doi: 10.1080/01431161.2020.1739353.
- [19] W. Wang and C. Cao, "NOAA-20 and S-NPP VIIRS Thermal Emissive Bands On-Orbit Calibration Algorithm Update and Long-Term Performance Inter-Comparison," *Remote Sens.*, vol. 13, no. 3, p. 448, Jan. 2021, doi: 10.3390/rs13030448.
- [20] W. Wang and C. Cao, "NOAA-20 VIIRS DNB Aggregation Mode Change: Pre-launch Efforts and On-Orbit Verification/Validation Results," *IEEE J. Sel. Top. Appl. Earth Obs. Remote Sens.*, vol. 12, no. 7, pp. 2015–2023, Jul. 2019, doi: 10.1109/JSTARS.2019.2898851.
- [21] J. Sun, M. Chu, and M. Wang, "On-orbit characterization of the VIIRS solar diffuser and attenuation screens for NOAA-20 using yaw measurements," *Appl. Opt.*, vol. 57, no. 22, p. 6605, Aug. 2018, doi: 10.1364/AO.57.006605.
- [22] T. J. Choi, S. Blonski, and C. Cao, "Initial on-orbit radiometric calibration of the NOAA-20 VIIRS Reflective Solar Bands," in *Proceedings of SPIE*, Sep. 2018, vol. 10764, p. 107641B. doi: 10.1117/12.2321752.
- [23] N. Lei, K. Twedt, X. Chen, and X. Xiong, "Initial radiometric calibration status and performance of NOAA-20 VIIRS reflective solar bands," in *Proceedings of SPIE*, Oct. 2018, vol. 10781, p. 107810M. doi: 10.1117/12.2324523.
- [24] H. Oudrari *et al.*, "JPSS-1 VIIRS Radiometric Characterization and Calibration Based on Pre-Launch Testing," *Remote Sens.*, vol. 8, no. 1, p. 41, Jan. 2016, doi: 10.3390/rs8010041.
- [25] D. Moyer, F. De Luccia, and E. Haas, "JPSS-1 VIIRS reflective solar band on-orbit calibration performance impacts due to SWIR nonlinearity artifacts," in *Proceedings of SPIE*, Oct. 2016, vol. 10000, p. 1000014. doi: 10.1117/12.2240126.
- [26] J. Sun, M. Chu, and M. Wang, "Degradation nonuniformity in the solar diffuser bidirectional reflectance distribution function," *Appl. Opt.*, vol. 55, no. 22, p. 6001, Aug. 2016, doi: 10.1364/AO.55.006001.
- [27] N. Lei and X. Xiong, "Impacts of the Angular Dependence of the Solar Diffuser BRDF Degradation Factor on the SNPP VIIRS Reflective Solar Band On-Orbit Radiometric Calibration," *IEEE Trans. Geosci. Remote Sens.*, vol. 55, no. 3, pp. 1537–1543, Mar. 2017, doi: 10.1109/TGRS.2016.2626963.
- [28] N. Lei and X. Xiong, "Determination of the solar angular dependence of the NOAA-20 VIIRS solar diffuser BRDF on-orbit change factor," in *Proceedings of SPIE*, Sep. 2019, vol. 11127, p. 111271Q. doi: 10.1117/12.2529783.
- [29] X. Xiong, N. Chen, Y. Li, and T. Wilson, "Assessments and applications of Terra and Aqua MODIS on-orbit electronic calibration," in *Proceedings of SPIE*, Sep. 2016, vol. 9972, p. 99720X. doi: 10.1117/12.2238603.
- [30] X. Xiong, J. Sun, J. Fulbright, Z. Wang, and J. J. Butler, "Lunar Calibration and Performance for S-NPP VIIRS Reflective Solar Bands," *IEEE Trans. Geosci. Remote Sens.*, vol. 54, no. 2, pp. 1052–1061, Feb. 2016, doi: 10.1109/TGRS.2015.2473665.
- [31] H. H. Kieffer and T. C. Stone, "The Spectral Irradiance of the Moon," *Astron. J.*, vol. 129, no. 6, pp. 2887–2901, Jun. 2005, doi: 10.1086/430185.
- [32] K. A. Twedt, N. Lei, and X. J. Xiong, "On-orbit noise characterization of the SNPP VIIRS reflective solar bands," in *Proceedings of SPIE*, Sep. 2017, vol. 10402, p. 104021X. doi: 10.1117/12.2274025.
- [33] N. Lei, K. Twedt, J. McIntire, and X. Xiong, "SNPP VIIRS RSB earth view reflectance uncertainty," in *2017 IEEE International Geoscience*



and Remote Sensing Symposium (IGARSS), Jul. 2017, pp. 5916–5919. doi: 10.1109/IGARSS.2017.8128355.

- [34] V. Murgai, L. Johnson, and E. M. Moskun, “BRDF characterization of solar diffuser for JPSS J1 using PASCAL,” in *Proceedings of SPIE*, Oct. 2014, vol. 9218, p. 921812. doi: 10.1117/12.2063153.
- [35] X. Xiong *et al.*, “Updates of Moderate Resolution Imaging Spectroradiometer on-orbit calibration uncertainty assessments,” *J. Appl. Remote Sens.*, vol. 12, no. 03, p. 1, Jul. 2018, doi: 10.1117/1.JRS.12.034001.
- [36] J.-L. Roujean, M. Leroy, and P.-Y. Deschamps, “A bidirectional reflectance model of the Earth’s surface for the correction of remote sensing data,” *J. Geophys. Res.*, vol. 97, no. D18, p. 20455, 1992, doi: 10.1029/92JD01411.
- [37] Q. Mu, A. Wu, X. Xiong, and A. Angal, “Assessment of SNPP VIIRS RSB detector-to-detector differences using deep convective clouds and deserts,” *J. Appl. Remote Sens.*, vol. 14, no. 01, p. 1, Feb. 2020, doi: 10.1117/1.JRS.14.018503.
- [38] S. Li, X. Xiong, and N. Lei, “S-NPP and N20 VIIRS RSB bands detector-to-detector calibration differences assessment using a homogeneous ground target,” in *Proceedings of SPIE*, Aug. 2020, vol. 11501, p. 115011N. doi: 10.1117/12.2568694.
- [39] X. Xiong *et al.*, “MODIS and VIIRS Calibration and Characterization in Support of Producing Long-Term High-Quality Data Products,” *Remote Sens.*, vol. 12, p. 3167, 2020, doi: 10.3390/rs12193167.
- [40] K. Meyer, S. Platnick, R. Holz, S. Dutcher, G. Quinn, and F. Nagle, “Derivation of Shortwave Radiometric Adjustments for SNPP and NOAA-20 VIIRS for the NASA MODIS-VIIRS Continuity Cloud Products,” *Remote Sens.*, vol. 12, no. 24, p. 4096, Dec. 2020, doi: 10.3390/rs12244096.
- [41] W. Wang and C. Cao, “Evaluation of NOAA-20 VIIRS Reflective Solar Bands Early On-Orbit Performance Using Daily Deep Convective Clouds Recent Improvements,” *IEEE J. Sel. Top. Appl. Earth Obs. Remote Sens.*, vol. 13, pp. 3975–3985, 2020, doi: 10.1109/JSTARS.2020.3007863.
- [42] S. Uprety, C. Cao, and X. Shao, “Radiometric performance characterization of NOAA-20 VIIRS reflective solar bands,” in *Proceedings of SPIE*, Sep. 2020, vol. 11501, p. 1150115. doi: 10.1117/12.2568721.
- [43] D. Moyer *et al.*, “JPSS-1VIIRS Prelaunch Polarization Testing and Performance,” *IEEE Trans. Geosci. Remote Sens.*, vol. 55, no. 5, pp. 2463–2476, May 2017, doi: 10.1109/TGRS.2016.2645403.
- [44] J. McIntire *et al.*, “Monochromatic measurements of the JPSS-1 VIIRS polarization sensitivity,” *Appl. Opt.*, vol. 55, no. 27, p. 7444, Sep. 2016, doi: 10.1364/AO.55.007444.
- [45] J. Sun, M. Wang, L. Jiang, and X. Xiong, “NOAA-20 VIIRS polarization effect and its correction,” *Appl. Opt.*, vol. 58, no. 24, p. 6655, Aug. 2019, doi: 10.1364/AO.58.006655.
- [46] K. A. Twedt, N. Lei, and X. Xiong, “Using solar eclipse events to validate VIIRS reflective solar band calibration at multiple radiance levels,” in *Proceedings of SPIE*, Oct. 2019, vol. 11151, p. 111511M. doi: 10.1117/12.2532855.
- [47] C. Moeller, T. Schwarting, J. McIntire, D. I. Moyer, and J. Zeng, “JPSS-1 VIIRS version 2 at-launch relative spectral response characterization and performance,” in *Proceedings of SPIE*, Sep. 2016, vol. 9972, p. 997203. doi: 10.1117/12.2238050.
- [48] K. A. Twedt, N. Lei, and X. Xiong, “On-orbit tracking of sub-sample gain differences in SNPP and NOAA-20 VIIRS imagery bands,” in *Proceedings of SPIE*, Oct. 2019, vol. 11151, p. 111512B. doi: 10.1117/12.2533125.



**Kevin A. Twedt** received the B.S. degree in physics from the University of Northern Iowa, Cedar Falls, IA, USA in 2004, and the Ph.D. degree in physics from the University of Maryland, College Park, MD, USA in 2012. He has performed experimental research in atomic physics, laser cooling, and focused ion beams at the University of Maryland and the National

Institute of Standards and Technology, Gaithersburg, MD, USA. He is currently a Lead Research Scientist with Science

Systems and Applications Inc., Lanham, MD, USA working on calibration of the MODIS and VIIRS instruments in support of the NASA Goddard Space Flight Center.



**Ning Lei** received the B. S. degree in physics from Fudan University, Shanghai, China, and the Ph.D. degree in physics from Rutgers University, The State University of New Jersey, New Brunswick, New Jersey, USA. He is a Lead Research Scientist with the VIIRS Characterization Support Team in the Science Systems and Applications, Inc., Lanham, MD, USA.



**Xiaoxiong (Jack) Xiong** received the B.S. degree in optical engineering from the Beijing Institute of Technology, Beijing, China, in 1982, and the Ph.D. degree in physics from the University of Maryland, College Park, MD, USA, in 1991.

He had worked in the fields of optical instrumentation, nonlinear optics, laser and atomic spectroscopy, and resonance ionization mass spectrometry at universities, industry, and at the National Institute of Standards and Technology (NIST), Gaithersburg, MD, USA. He is an Optical Physicist with the NASA Goddard Space Flight Center (GSFC), Greenbelt, MD, USA. He is also serving as the Moderate-Resolution Imaging Spectroradiometer (MODIS) Project Scientist and the Technical Lead for both the MODIS Characterization Support Team (MCST) and the VIIRS Calibration Support Team (VCST).

**Amit Angal** is currently a Lead Optical Engineer and a Supervisor with the Science Systems and Applications, Inc., Lanham, MD, USA, where he is involved in the radiometric characterization and calibration of remote sensing instruments. He is primarily involved in the on-orbit calibration of the reflective solar bands of the Moderate Resolution Imaging Spectroradiometer (MODIS) instruments on-board the Terra and Aqua Spacecraft. He has also supported the CLARREO Mission Preformulation activities in the reflective solar spectrum. In addition, he supports the preflight calibration of the JPSS Visible Infrared Imaging Radiometer Suite (VIIRS) instruments and is involved in the on-orbit calibration and validation of the SNPP and NOAA-20 VIIRS instruments. His research interest includes cross-calibration between Landsat and MODIS instruments.

**Sherry Chen Xuexia Li** received the B.S. degree in geography and the M.S. degree in environmental sciences from Peking University, Beijing, China, and the Ph.D. degree in atmosphere, environment, and water resources from the South Dakota School of Mines and Technology, Rapid City, SD, USA. From 2000 to 2012, she has worked on multiple research projects, such as USGS LANDFIRE (Landscape Fire and Resource Management Planning Tools) project, Peru Hydropower Assessment, Land Cover Change, Biomass Estimation, and a Tethered Balloon (SWAMI: Short-Wave Aerostat Mounted Imager) Remote Sensing platform. She is currently a Senior



Research Scientist with Science Systems and Applications, Inc., Lanham, MD, USA. Since 2012, she has been working with the Moderate Resolution Imaging Spectroradiometer (MODIS) and Visible Infrared Imaging Radiometer Suite (VIIRS) Characterization Support Teams. Her work focuses on MODIS and VIIRS calibration and multiple sensors' intercomparisons.



**Tiejun Chang** received a M.S. degree in Computer Science from Montana State University, and a Ph.D. degree in Optics from University of Paris-Sud, France. His work focuses on radiometric calibration and validation of satellite remote sensors, and he has experience on MODIS, VIIRS, AVHRR, and GOES-R/ABI. He is working with the MODIS and VIIRS Characterization and Support Teams at the National Aeronautics and Space Administration (NASA), Goddard Space Flight Center (GSFC).



**Junqiang Sun** is currently a chief research scientist at Science Systems and Applications, Inc. (SSAI) in Lanham, MD serving as team leader for the VIIRS Characterization Support Team (VCST) to work on VIIRS instrument calibration and characterization and also serving as instruments calibration lead to work on MODIS instrument calibration and characterization. He received the B.S. degree in physics from Changsha Institute of Technology, Changsha, China, and PhDs. in physics and chemistry from the University of Science and Technology of China, Hefei, China, and from University of Florida, Gainesville, FL, respectively. Dr. Sun has previously worked at Global Science and Technology, Inc. (GST), Greenbelt, MD and Sigma Space Corporation, Lanham, MD as a principal scientist and as a chief support scientist on MODIS and VIIRS calibration and characterization, respectively. Before working in the space industry, Dr. Sun had extensively worked in atomic and molecular physics and in quantum chemistry for over a decade.